Journal of
Materials Chemistry C

PAPER

Cite this: *J. Mater. Chem. C*, 2017, 5, 370

In-plane isotropic charge transport characteristics of single-crystal FETs with high mobility based on 2,6-bis(4-methoxyphenyl)anthracene: experimental cum theoretical assessment†

Aiyuan Li,‡[a] Lijia Yan,‡[b] Chao He,[a] Yanan Zhu,[a] Dongwei Zhang,[a] Imran Murtaza,[b] Hong Meng*[ab] and Osamu Goto*[a]

Received 27th October 2016,
Accepted 28th November 2016

DOI: 10.1039/c6tc04659b

www.rsc.org/MaterialsC

In-plane isotropic charge transport in single crystals is desirable in large-area single-crystal thin-film transistor (FET) arrays because it is independent of crystal direction. However, most organic semiconductors show anisotropic charge transport, while only a few show isotropic or moderately isotropic charge transport characteristics. We report a highly isotropic charge transport semiconductor material, 2,6-bis(4-methoxyphenyl)anthracene (BOPAnt), and demonstrate BOPAnt-based single-crystal FETs with a high mobility of 13–16 cm^2 V^{-1} s^{-1} and an anisotropic mobility ratio (μ_{max}/μ_{min}) of approximately 1.23, the lowest value yet reported. Using the single-crystal structure of BOPAnt, the rectangular diffraction patterns of the molecular lattice parameters in single-crystal thin films were analysed by transmission electron microscopy and polarized optical microscopy. The highly isotropic properties are attributed to the molecular structure enhancement by incorporation of methoxyphenyl units; our analysis revealed an orthorhombic lattice arrangement in the solid state, with the molecules packed in an unusual fashion in this particular stacking mode. In addition, hole mobility calculations combining the transfer integrals and the reorganization energy are used to explain the charge-transport properties.

Introduction

The absence of grain boundaries and the presence of highly ordered molecular structures in organic single crystals are extremely useful for exploring the intrinsic properties of a material. Very high-field effect mobilities of both p-type and n-type materials can be obtained using single-crystal thin-film transistors (TFTs).[1–5] Although high-mobility organic TFTs (OTFTs) have been fabricated based on polymers[6,7] or small molecules,[8–11] these OTFTs still require complex processing to control their molecular alignment, and they suffer from instability. The mobility of a single crystal-based FET is much higher than that of the corresponding thin-film FET; thus, single-crystal FETs constitute a competitive technology candidate for large-area flexible electronics applications.

Elucidating the relationship between molecular packing and charge-transport properties would be very interesting and would provide valuable feedback to guide the design of new materials. The charge-transport properties are strongly influenced by the molecular packing direction in single-crystal FET devices; therefore, studying orientation-dependent charge-transport characteristics is important. Notably, most organic semiconductors have a weak charge transport along the direction perpendicular to the substrate. Such weak transport is determined by their weak molecular interactions in this direction. Unless specifically noted, orientation-dependent charge transport is confined to the two dimensions that are parallel to the substrate. In such studies, single-crystal FET devices are fabricated with channels in different crystallographic directions, and the ratio between the highest and lowest mobility (μ_{max}/μ_{min}) or between the long- and short-axis channel mobilities is used to express the extent of anisotropy. Most organic semiconductors, such as rubrene,[12] pentacene,[13] tetracene[14] and some nano-ribbon single-crystal materials,[15] show anisotropic charge-transport characteristics. The anisotropic μ_{max}/μ_{min} ratios of these materials reportedly range from 2 to greater than 100. Many reports have addressed large-area, single-crystal TFT arrays.[16–19] In such studies, single crystals can be grown at designated positions, but the orientation control of single crystals remains highly

---

[a] *School of Advanced Materials, Peking University Shenzhen Graduate School, Peking University, Shenzhen, 518055, China. E-mail: menghong@pkusz.edu.cn, ogoto@pkusz.edu.cn*

[b] *Key Laboratory of Flexible Electronics (KLOFE) & Institute of Advanced Materials (IAM), Jiangsu National Synergetic Innovation Center for Advanced Materials (SICAM), Nanjing Tech University (Nanjing Tech), 30 South Puzhu Road, Nanjing 211816, China*

† Electronic supplementary information (ESI) available. See DOI: 10.1039/c6tc04659b

‡ These authors contributed equally to this work.

problematic, and thus the potential of single-crystal FETs cannot be fully realized. Nonetheless, a few reports have focused on the isotropic or weakly anisotropic charge transport of single-crystal TFTs, as summarized in Table S1 (ESI†). Batlogg reported isotropic charge-transport single-crystal transistors based on dinaphtho-thieno-thiophene (DNTT),[20] which had $\mu_{\max}/\mu_{\min}$ ratios of 1.3–1.7 and mobilities approaching 10 cm^2 V^{-1} s^{-1}.[21] Bao *et al.* described end-capped [1]benzothieno[3,2-*b*]benzothiophene-based single-crystal FETs with a mobility of 17 cm^2 V^{-1} s^{-1}.[22] For this material, the transfer integrals in all directions were similar, molecular modelling results showed isotropic characteristics. Isotropic (weakly anisotropic) semiconductors have one common characteristic, strong and balanced electronic coupling in the molecular packing that provides sufficient charge transport in different crystallographic directions. Notably, there are no absolutely isotropic charge transport characteristics; when the ratio $\mu_{\max}/\mu_{\min}$ is lower than 1.5, the charge transport can be considered to be isotropic or weakly anisotropic. Such low anisotropy ratios are rare for organic semiconductors, which facilitate the future application of single-crystal FET arrays by eliminating the need to consider the effect of single-crystal growth orientation.

Anthracene derivatives, a class of organic semiconductors with excellent performance, have been used to fabricate TFT devices with high mobility and excellent stability.[23] These materials also show great potential as isotropic charge-transport semiconductors. In our previous work, we reported single-crystal transistors based on di(phenylvinyl)anthracene (DPVAnt) with μ_a/μ_b values of 1.5–1.9.[24] Following our report, Hu and colleagues recently reported 2,6-diphenyl anthracene (DPA) with both high mobility and high luminescence,[25,26] and their single-crystal TFTs showed the μ_c/μ_b values of 1.3 to 1.5. However, these devices were fabricated with ultra-thin wires as the shadow mask, and they only measured the devices in two directions. Additional crystallographic directions with higher-resolution single-crystal FET devices are needed to obtain more convincing results.

Recently, our group introduced different heteroatoms into the peripheral side chains of anthracene derivatives to tune their optical and electronic behaviours. As a result, the mobility of the evaporated TFTs exceeded 3.72 cm^2 V^{-1} s^{-1}.[27] In this report, we fabricated single-crystal FET devices based on 2,6-bis(4-methoxyphenyl)anthracene (BOPAnt) with both gold wire and fan-shaped shadow masks to study their orientation-dependent charge-transport characteristics. Both types of FETs show isotropic charge-transport characteristics, with $\mu_{\max}/\mu_{\min}$ (or μ_b/μ_a) values of approximately 1.2 and mobilities in the range of 13.4–16.6 cm^2 V^{-1} s^{-1}. To the best of our knowledge, the present communication presents the first example of a very high-charge-mobility organic semiconductor with isotropic behaviour.

Experimental

Single-crystal growth

BOPAnt was synthesized in-house according to a synthesis procedure described elsewhere.[27] The single crystals were grown *via* PVT using a horizontal tube furnace. The raw BOPAnt was purified three times by sublimation before single-crystal growth. During the 45 minute process of single-crystal growth, the raw material was placed in the sublimation regime and vapourized at 310 °C; the growth temperatures in zones 2 and 3 were 240 °C and 200 °C, respectively.

Device fabrication and characterization

As the substrate, *n*-Si wafers with 250 nm thermally grown silicon dioxide as the dielectric layer were used. They were ultrasonically cleaned with piranha solution, acetone and isopropyl alcohol (IPA). After cleaning, the substrates were surface-treated with OTS before device fabrication. The single-crystal TFTs were fabricated in a top contact/bottom gate configuration. The cleaned substrates were placed directly into the PVT growth zone to grow large and thin single crystals prior to shadow mask alignment under a microscope. Gold was evaporated to create the source and drain electrodes. The shadow masks used in this report were either gold wires or a fan-shaped shadow mask with a channel length of 50 μm.

The transfer and output characteristics of the TFT were characterized in air using an Agilent B1500A combined probe station. The carrier mobility (μ) was extracted using the equation $I_{\mathrm{sd}} = \mu C_{\mathrm{i}}(W/2L)(V_{\mathrm{g}} - V_{\mathrm{t}})^2$ under the saturation regime.

TEM, XRD, POM and thickness characterization

XRD data were obtained from single crystals grown directly on the SiO_2/Si substrate using a BrukerD8 Advance instrument. POM characterization was performed with a Shanghai BIMU Company XP-213, and TEM characterization was conducted with an FEI Tecnai G2F30. The thicknesses of the single-crystal films were measured using a Bruker Dektak XT Profilometer.

Theoretical modelling

All of the geometric optimizations of the monomer molecules and the reorganization energy calculations were conducted using the B3LYP functional set and the 6-31G(d) basis set. These calculations and the transfer integral calculations were performed using the Gaussian 09 package and J_from-g03 software. The reorganization energy consists of the inner sphere contribution and the outer sphere contribution. Here, we focused on the inner sphere, which represents the relaxation in the molecular geometry.

Results and discussion

Fig. 1(a) shows the BOPAnt molecular structure; the BOPAnt synthesis procedure has been reported elsewhere.[27] The torsion angles between the substituted phenyl groups and the anthracene core are 15.2° and 16.3°, and the planar molecular structure guarantees relatively strong intermolecular packing. Fig. 1(b) shows the single-crystal molecular stacking in the *a*–*b* plane, as derived from the cif file of the single-crystal X-ray diffraction (XRD) data.[24] The BOPAnt crystals belong to the *Pbca* space group of the orthorhombic crystal system, with unit cell parameters

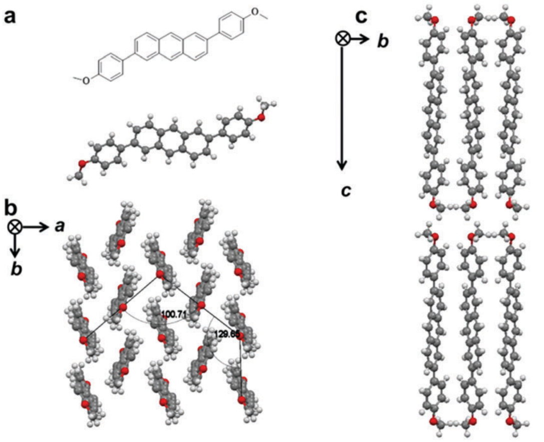

Fig. 1 (a) BOPAnt molecular structure; (b) and (c) BOPAnt molecular packing.

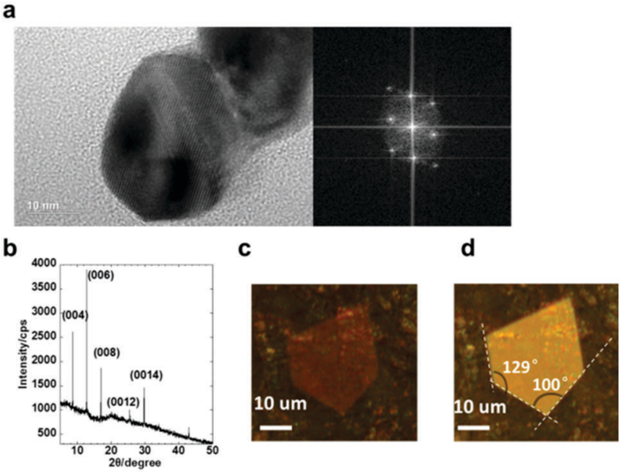

Fig. 2 (a) TEM image of a single BOPAnt crystal and its corresponding SAED spectrum; (b) powder XRD spectra of single crystals grown directly on the substrate. (c and d) POM images of BOPAnt single crystals.

a = 7.44 Å, b = 6.16 Å and c = 42.30 Å, $\alpha = \beta = \gamma = 90.0°$. Crystal structure analysis revealed that the BOPAnt molecules are packed with a herringbone geometry. The molecular packing of BOPAnt in the a–b plane shows that the angle between the $\{1\ {-1}\ 0\}$ and $\{-1\ {-1}\ 0\}$ facets is 100.7°, whereas that between the $\{-1\ {-1}\ 0\}$ and $\{1\ 0\ 0\}$ facets is 129.6°. Fig. 1(c) shows the molecular packing in the b–c plane; without sufficient π–π stacking, the interaction between the molecules along the c axis is very weak.

High-quality single crystals were grown by physical vapour transport (PVT), and the source material was purified three times by sublimation prior to use. A diagram of the instrument used to grow the single crystals in this work is shown in Fig. S1 (ESI†). The sublimation and growth temperatures were set at 320 °C and 240 °C, respectively, and the sublimation temperature was set according to the differential scanning calorimeter (DSC) data to prevent the material from melting.[24] The growth temperature was set below 250 °C to avoid the destruction of the octadecyltrichlorosilane (OTS)-treated surface. Using high sublimation and high growth temperatures, large and thin single crystals were grown directly on the OTS-treated SiO_2/Si substrates.

To further analyse the single-crystal structure and to assign the X-ray diffraction patterns of the molecular lattice parameters, transmission electron microscopy (TEM) was performed. Fig. 2(a) shows that the single crystal has typical facet angles, and the corresponding selected area electron diffraction (SAED) pattern clearly shows fringes and diffraction spots. No changes in the SAED pattern were observed in different parts of the image, confirming the growth of a single crystal.

Fig. 2(b) shows the indexed powder XRD spectra of the single crystals grown directly on the substrate; the spectra show (0 0 h) peaks, including 8.33° (0 0 4), 12.66° (0 0 6), 16.9° (0 0 8), 25.28° (0 0 12) and 29.52° (0 0 14), indicating that the single crystals were aligned along the c-axis on the substrates. The full width at half maximum (FWHM) values of these peaks are very small, indicating that high-quality single crystals were obtained with this method.

Fig. 2(c) and (d) show polarized optical microscopy (POM) images of the single crystals. While rotating the sample holder in the polarized mode, the crystals were observed to exhibit uniform colour and to change from dark to bright.

Single-crystal TFTs were fabricated using ultra-thin wires as the shadow mask, and a POM image of the resulting device and its characteristics are shown in Fig. S2 (ESI†). The characteristics of a TFT with channel lengths of 50 μm along the a and b axes were measured. The results showed that the anisotropy ratio μ_a/μ_b was 1.24 (Table S2, ESI†), indicating that this material may have isotropic charge-transport characteristics. To further analyse the orientation-dependent charge-transport characteristics, several TFT devices that continuously ranged from the a-axis to the b-axis were required.

We grew large, thin single crystals by combining PVT with a precise fan-shaped shadow mask to obtain FETs with different orientations. The single crystals were grown directly on the OTS-treated SiO_2/Si substrates, as discussed previously, and the molecules were packed along the c-axis, perpendicular to the substrate. The FET devices were fabricated with regularly shaped single crystals, and the orientations of the single crystals, *i.e.*, along the a and b axes, can be identified according to the conservation law of the crystal face angle, as shown in Fig. 3(a). The W and L values as well as the facet angle were measured using POM software, as shown in the Fig. S3 (ESI†). The W value for each FET is calculated using $W = (W_1 + W_2)/2$, the L value is about 50 μm as determined by the fan shaped shadow mask. The device characteristics were measured using an Agilent B1500A. The transfer characteristics were measured under $V_d = -80$ V, and the saturation mobility values at different positions are shown in Fig. 3(b). The anisotropy ratio of the highest mobility to the lowest mobility, *i.e.*, μ_{max}/μ_{min} = 1.23, indicates that the BOPAnt single crystal shows isotropic charge-transport characteristics. The device performance data are listed in Table 1 and showed highest maximal mobility of 16.6 $cm^2\ V^{-1}\ s^{-1}$. Although the single crystal was not large enough to fully cover the fan-shaped shadow mask, the molecular packing was symmetrical, and all the crystallographic directions

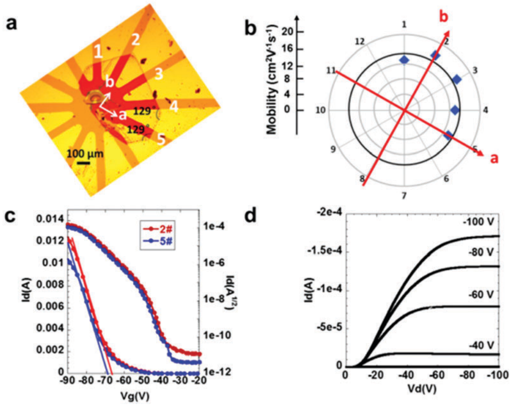

Fig. 3 (a) POM image of BOPAnt single-crystal transistors obtained with a fan-shaped shadow mask in different orientations. (b) Mobility values along different directions. (c) Transfer curves of FETs with channels along the *a*-axis (2#) and the *b*-axis (5#). (d) Output characteristics of TFT 5.

Table 1 Device performance of single-crystal TFTs along different crystallographic directions. All devices were measured under $V_d = -80$ V

Device	Mobility (cm^2 V^{-1} s^{-1})	*V*th (V)	On/off ratio
1	13.1	−63.0	2.70×10^7
2	16.6	−65.0	2.72×10^7
3	16.0	−63.0	9.33×10^6
4	13.5	−63.0	4.61×10^7
5	13.4	−65.0	6.00×10^7

ranging from the *a*-axis to the *b*-axis were included in these devices. Therefore, we conclude that high-mobility isotropic characteristics were obtained.

Fig. 3(c) shows the transfer characteristic curves of the TFTs with channels along the *a* and *b* axes, *i.e.*, TFT devices 2 and 5, respectively. The mobilities of the two devices were 16.0 cm^2 V^{-1} s^{-1} and 13.4 cm^2 V^{-1} s^{-1}, respectively; the on/off ratio exceeded 10^7, and the threshold voltage was approximately −68 V. The voltage dependence of the mobility, as evident in the $I_d^{1/2} \sim V_g$ curve, may be attributable to the contact resistance,[28] as the highest occupied molecular orbital (HOMO) level of the BOPAnt was electrochemically determined to be −5.45 eV,[24] and the work function of Au is −5.1 eV. As a result, a 0.35 eV barrier exists at the interface between the Au and the single crystal. The contact-resistance problem also influenced the $I_d \sim V_d$ curve in Fig. 3d, as indicated by the slow enhancement of the I_d current in the low-V_d region. The device was fabricated and measured under ambient conditions. The measurement was taken under a humidity of around 65%, causing more traps in the single crystal/substrate interface, thus the *V*th value is quite high.[29]

The *I*–*V* curves of the FET without applying V_g are shown in the Fig. S4 (ESI†). It is difficult to determine the charge transport behavior from the results at $V_g = 0$, since the current is very low and the measurement is not taken in the clean room or N_2 glove box, so we cannot exclude the noise from the surroundings.

In addition, we constructed several other devices with large single crystals, using different types of shadow masks, to fabricate single-crystal TFTs with different orientations. The results are shown in Fig. S5 and Table S3 (ESI†). Those results also show isotropic charge transport characteristics, with $\mu_{\max}/\mu_{\min} = 2.90/1.99 = 1.45$.

The transfer integrals and the reorganization energies for different crystallographic directions[24] are used to further analyse the relationship between the molecular structure of a material and its resulting properties. The hopping mode is always used to explain organic semiconductor charge transport, and the mobility is strongly influenced by the electronic coupling of the molecules, which is reflected in the dimer transfer integrals along different crystallographic directions. Although the organic semiconductor charge transport mechanism remains highly debated, and the theoretical models still need improvement, they may be used as references to explain the charge transport behaviour of organic semiconductors.

The transfer integrals in the *a*–*b* plane are shown in Fig. 4(a). The transfer integrals are sensitive to the distance between dimers and can determine the charge transport in a specific direction. The value along the diagonal directions is approximately 75.5 meV, while the dimers along the *b*-axis exhibit values of 13.35 meV. The dimer spacing increases along the *c* direction; the transfer integrals in this direction are extremely small and are not shown here. The angle between the diagonal lines is 81.6°. Using the Marcus–Levich–Jortner simulations,[22,30] the mobility values along different crystallographic directions were calculated, and the results are shown in Fig. 4(b). The mobility calculated by the transfer integrals *P*, T_1 and T_2 are shown in Table S4 (ESI†). Although the transfer integral of *P* is not small, when combined with the reorganization energy and molecular distance, the calculated mobility with the transfer integral *P* is only 0.19% of the mobility with the transfer integrals T_1 and T_2, indicating that the contribution of P can be ignored. Thus, the mobilities for different orientations are mainly determined by the transfer integrals T_1 and T_2, which constitute a strong and balanced electronic coupling.

This strong and balanced electronic coupling can also be verified by the shape of the single crystal, as the molecular interactions in different crystallographic directions determine the growth speed of the facet. As an extreme example, the nano-ribbon shape has the

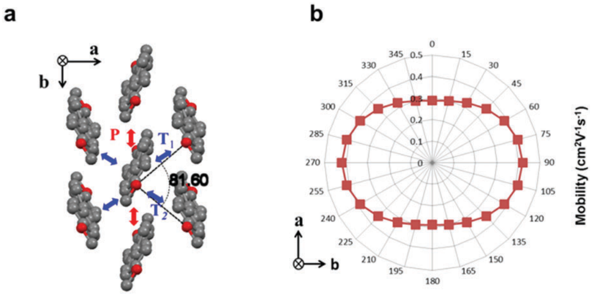

Fig. 4 (a) Transfer integrals in the *a*–*b* plane of BOPAnt molecular packing 27 and transfer integrals along the diagonal (blue) (*i.e.*, T_1 and T_2) are approximately 72.5 meV. The dimers along the *b* axis direction (red) (*i.e.*, *P*) are 13.35 meV, and the angle between the two diagonal lines is 81.6°. (b) The calculated orientation-dependent hole-transport mobilities.

strongest molecular interactions along the long axis; thus, mobility is much higher along the long axis than the short axis.[15,30] The relationship between charge transport mobility and facet growth rate was also clarified by examining three-dimensional charge transport characteristics, where the charge mobility in one direction is in accord with the corresponding dimension.[31] During the growth of BOPAnt, the single crystals appeared as regular parallelograms; a typical single crystal grown in zone 3 is shown in Fig. S6 (ESI†), where the ratio of the growth speed along the *a* and *b* axes was 1.11. These facets were still clearly seen in crystals grown in zone 2, which has a higher temperature; here, the ratio of the growth speed along the *a* and *b* axes was 1.03, as shown in Fig. 3(a). The balanced growth speed along different crystallographic directions indicates that there is also balanced electronic coupling in different crystallographic directions, which is required for isotropic charge transport.

To further explore the intrinsic charge transport characteristics, as an extension of the current work, we will measure the orientation dependent charge transport under different temperatures.

Conclusions

In conclusion, we have fabricated BOPAnt-based single-crystal FET devices using both gold wires and a fan-shaped shadow mask. The results obtained using both methods indicate isotropic charge transport with the excellent anisotropic μ_a/μ_b ratios of 1.24 (gold wire devices) and 1.23 (fan-shaped devices), with the maximal mobility of 16.6 cm^2 V^{-1} s^{-1} representing the highest mobility yet reported. Theoretical modelling supplements our experimental results, which confirm the promise of BOPAnt semiconductors for large-area, single-crystal FET arrays because they overcome the difficulty in controlling single-crystal growth orientation. The innovative structural design strategy enables the design of a new series of highly isotropic materials for their further utilization in organic optoelectronic devices.

Conflict of interest

The authors declare no competing financial interest.

Acknowledgements

This work was financially supported by the Shenzhen Key Laboratory of Organic Optoelectromagnetic Functional Materials of the Shenzhen Science and Technology Plan (ZDSYS20140509094114164), the Shenzhen Peacock Program (KQTD2014062714543296), a Shenzhen Science and Technology research grant (JCYJ20140509093817690 and JCYJ20150331100628880), a Nanshan Innovation Agency grant (No. KC2015ZDYF0016A), the Guangdong Key Research Project (No. 2014B090914003 and 2015B090914002), the Guangdong Talents Project (51035008), the National Basic Research Program of China (973 Program, No. 2015CB856505), the Postgraduate Innovation Foundation of Jiangsu Province (2014, KYLX_0773) and the Guangdong Academician Workstation (2013B090400016).

Notes and references

1 O. D. Jurchescu, J. Baas and T. T. M. Palstra, *Appl. Phys. Lett.*, 2004, **84**, 3061–3063.
2 C. Liu, T. Minari, X. Lu, A. Kumatani, K. Takimiya and K. Tsukagoshi, *Adv. Mater.*, 2011, **23**, 523–526.
3 V. Podzorov, S. E. Sysoev, E. Loginova, V. M. Pudalov and M. E. Gershenson, *Appl. Phys. Lett.*, 2003, **83**, 3504–3506.
4 N. A. Minder, S. Ono, Z. H. Chen, A. Facchetti and A. F. Morpurgo, *Adv. Mater.*, 2012, **24**, 503–508.
5 J. Takeya, M. Yamagishi, Y. Tominari, R. Hirahara, Y. Nakazawa, T. Nishikawa, T. Kawase, T. Shimoda and S. Ogawa, *Appl. Phys. Lett.*, 2007, **90**, 182117.
6 C. Luo, A. K. K. Kyaw, L. A. Perez, S. Patel, M. Wang, B. Grimm, G. C. Bazan, E. J. Kramer and A. J. Heeger, *Nano Lett.*, 2014, **14**, 2764–2771.
7 H. R. Tseng, L. Ying, B. B. Y. Hsu, L. A. Perez, C. J. Takacs, G. C. Bazan and A. J. Heeger, *Nano Lett.*, 2012, **12**, 6353–6357.
8 Y. B. Yuan, G. Giri, A. L. Ayzner, A. P. Zoombelt, S. C. B. Mannsfeld, J. H. Chen, D. Nordlund, M. F. Toney, J. S. Huang and Z. N. Bao, *Nat. Commun.*, 2014, **5**, 3005.
9 H. Iino, T. Usui and J. Hanna, *Nat. Commun.*, 2015, **6**, 6828.
10 Y. He, M. Sezen, D. Zhang, A. Li, L. Yan, H. Yu, C. He, O. Goto, Y.-L. Loo and H. Meng, *Adv. Electron. Mater.*, 2016, **2**, 1600179.
11 Y. He, W. Xu, I. Murtaza, D. Zhang, C. He, Y. Zhu and H. Meng, *RSC Adv.*, 2016, **6**, 95149–95155.
12 R. Zeis, C. Besnard, T. Siegrist, C. Schlockermann, X. L. Chi and C. Kloc, *Chem. Mater.*, 2006, **18**, 244–248.
13 J. Y. Lee, S. Roth and Y. W. Park, *Appl. Phys. Lett.*, 2006, **88**, 252106.
14 Y. Xia, V. Kalihari, C. D. Frisbie, N. K. Oh and J. A. Rogers, *Appl. Phys. Lett.*, 2007, **90**, 162106.
15 S. Choi, S. H. Chae, M. H. Hoang, K. H. Kim, J. A. Huh, Y. Kim, S. J. Kim, D. H. Choi and S. J. Lee, *Chem. – Eur. J.*, 2013, **19**, 2247–2251.
16 O. Goto, S. Tomiya, Y. Murakami, A. Shinozaki, A. Toda, J. Kasahara and D. Hobara, *Adv. Mater.*, 2012, **24**, 1117–1122.
17 A. L. Briseno, S. C. B. Mannsfeld, M. M. Ling, S. Liu, R. J. Tseng, C. Reese, M. E. Roberts, Y. Yang, F. Wudl and Z. Bao, *Nature*, 2006, **444**, 913–917.
18 H. Minemawari, T. Yamada, H. Matsui, J. y. Tsutsumi, S. Haas, R. Chiba, R. Kumai and T. Hasegawa, *Nature*, 2011, **475**, 364–367.
19 K. Nakayama, Y. Hirose, J. Soeda, M. Yoshizumi, T. Uemura, M. Uno, W. Li, M. J. Kang, M. Yamagishi, Y. Okada, E. Miyazaki, Y. Nakazawa, A. Nakao, K. Takimiya and J. Takeya, *Adv. Mater.*, 2011, **23**, 1626–1629.
20 W. Xie, K. Willa, Y. F. Wu, R. Hausermann, K. Takimiya, B. Batlogg and C. D. Frisbie, *Adv. Mater.*, 2013, **25**, 3478–3484.
21 M. Uno, Y. Tominari, M. Yamagishi, I. Doi, E. Miyazaki, K. Takimiya and J. Takeya, *Appl. Phys. Lett.*, 2009, **94**, 223308.
22 G. Schweicher, V. Lemaur, C. Niebel, C. Ruzie, Y. Diao, O. Goto, W. Y. Lee, Y. Kim, J. B. Arlin, J. Karpinska,

A. R. Kennedy, S. R. Parkin, Y. Olivier, S. C. B. Mannsfeld, J. Cornil, Y. H. Geerts and Z. N. Bao, *Adv. Mater.*, 2015, **27**, 3066–3072.

23 J. Li, J. Liu, Y. G. Zhen, L. Q. Meng, Y. Wang, H. L. Dong and W. P. Hu, *J. Mater. Chem. C*, 2015, **3**, 10695–10698.

24 H. Y. Li, B. C. K. Tee, G. Giri, J. W. Chung, S. Y. Lee and Z. N. Bao, *Adv. Mater.*, 2012, **24**, 2588–2591.

25 J. Liu, H. T. Zhang, H. L. Dong, L. Q. Meng, L. F. Jiang, L. Jiang, Y. Wang, J. S. Yu, Y. M. Sun, W. P. Hu and A. J. Heeger, *Nat. Commun.*, 2015, **6**, 10032.

26 J. Liu, H. L. Dong, Z. R. Wang, D. Y. Ji, C. L. Cheng, H. Geng, H. T. Zhang, Y. G. Zhen, L. Jiang, H. B. Fu, Z. S. Bo, W. Chen, Z. G. Shuai and W. P. Hu, *Chem. Commun.*, 2015, **51**, 11777–11779.

27 L. Yan, Y. Zhao, H. Yu, Z. Hu, Y. He, A. Li, O. Goto, C. Yan, T. Chen, R. Chen, Y.-L. Loo, D. F. Perepichka, H. Meng and W. Huang, *J. Mater. Chem. C*, 2016, **4**, 3517–3522.

28 D. Braga and G. Horowitz, *Adv. Mater.*, 2009, **21**, 1473–1486.

29 D. Li, E. Borkent, R. Nortrup, H. Moon, H. Katz and Z. Bao, *Appl. Phys. Lett.*, 2005, **86**, 042105.

30 V. Coropceanu, J. Cornil, D. A. da Silva, Y. Olivier, R. Silbey and J. L. Bredas, *Chem. Rev.*, 2007, **107**, 926–952.

31 T. He, X. Y. Zhang, J. Jia, Y. X. Li and X. T. Tao, *Adv. Mater.*, 2012, **24**, 2171–2175.